A Mesoscale Numerical Model Using the Nonhydrostatic Pressure-based Sigma-Coordinate Equations: Model Experiments with Dry Mountain Flows

MING XUE* AND ALAN J. THORPE

Department of Meteorology, University of Reading, United Kingdom

(Manuscript received 5 March 1990, in final form 12 October 1990)

ABSTRACT

A nonhydrostatic numerical model suitable for simulating mesoscale meteorological phenomena is developed and described here. The model is the first to exploit the nonhydrostatic equation system in σ (normalized pressure) coordinates. In addition to the commonly recognized advantages of σ-coordinate models, this model is potentially advantageous in nesting with large-scale σ-coordinate models. The equation system does not support sound waves but it presents the internal gravity waves accurately. External gravity waves are the fastest wave modes in the system that limit the integration time step. However, since short nonhydrostatic external waves are much slower than the speed of shallow-water waves and because fast hydrostatic long waves imposes less severe restriction on the time step when they are resolved by many grid points, a large time step (compared to that determined by the speed of hydrostatic shallow-water waves) can be used when horizontal grid spacing is on the order of 1 km.

The system is solved in a way analogous to the anelastic system in terrain-following height coordinates. The geopotential height perturbation is diagnosed from an elliptic equation. Conventional finite-differencing techniques are used based on Arakawa C grid. The flux-corrected transport (FCT) scheme is included as an option for scalar advection.

The model has been used to study a variety of problems and here the simulations of dry mountain waves are presented. The results of simulations of the 11 January 1972 Boulder severe downslope windstorm are reported and the wave development mechanism discussed.

1. Introduction

Pressure has been widely used as a vertical coordinate in modeling and theoretical studies of large-scale hydrostatic flows ever since the pioneering work of Eliassen (1949), the difficulties with the lower boundary is circumvented by using the normalized pressure σ as the vertical coordinate (Phillips 1957). Pressure-based coordinate systems are employed in essentially all current limited-area and global-scale numerical models for meteorological applications. The advantages of this are generally recognized. Using pressure as an independent variable eliminates the not routinely observed air density from the governing equations and simplifies thermodynamic calculations. Furthermore, numerical models in such a coordinate system can easily incorporate observational data that are generally available at pressure levels. The σ-coordinate system is also used in certain mesoscale numerical models (e.g., Anthes and Warner 1978), but they are all hydrostatic.

On the other hand, almost all nonhydrostatic meteorological models use height as the vertical coordinate. Most of such models (e.g., Wilhelmson and Ogura 1972; Clark, 1977) are based on the anelastic equation system as derived by Ogura and Phillips (1962). The fully compressible equation set in height coordinates is also used in small-to-mesoscale models (e.g., Klemp and Wilhelmson 1978; Tapp and White 1976). In the former, a mode-splitting technique is used to deal with sound waves. But still the overall performance is limited by the small time steps required by fast sound waves.

In the mid-seventies, Miller (1974) derived a set of equations that is nonhydrostatic but uses pressure as the vertical coordinate. A three-dimensional cloud model was developed based on this equation system (Miller and Pearce 1974), which was successfully used in many modeling studies on convective systems (e.g., Moncrieff and Miller 1976; Thorpe et al. 1982). Recently, Miller and White (1984, MW84 hereafter) presented a more rigorous derivation of that equation set based on a systematic scale analysis and power series expansion. An equation set in σ coordinates was obtained by direct transformation from the pressure coordinate system. The work of MW84 lays the foundation for the numerical model to be described in this paper.

A nonhydrostatic model in pressure-based σ coordinates bears all the advantages of its hydrostatic coun-

---

* *Current affiliation*: Center for the Analysis and Prediction of Storms, University of Oklahoma, Norman, Oklahoma.

Corresponding author address: Dr. Ming Xue, Center for the Analysis and Prediction of Storms, The University of Oklahoma, Norman, OK 73019-0515.

terpart, and further it has the potential advantage in internesting with hydrostatic regional or global scale σ-coordinate models. The nonhydrostatic σ-coordinate system is also soundproof.

In this paper, a new mesoscale numerical model based on this equation system is described. The model is capable of dealing with an irregular terrain and has been used to study convective processes. In section 2, a brief introduction to the σ-coordinate nonhydrostatic equations is presented, and in section 3 the numerical formulation of the model is described. In section 4 the model solutions of dry mountain waves are shown, as well as the results of the simulations of the 11 January 1972 Boulder, Colorado, severe downslope windstorm. A summary is given in section 5.

2. The nonhydrostatic equation system in σ coordinates

a. The equations

A nonhydrostatic approximate equation set in pressure coordinates was devised by Miller (1974) and used successfully by Miller and Pearce (1974) to formulate a 3D numerical cloud model. The feasibility of nonhydrostatic equations in a pressure-based vertical coordinate can be briefly illustrated. We define a quantity

$$\epsilon \equiv \frac{1}{g}\frac{dw}{dt} = g^{-2}\frac{d}{dt}\left(\frac{d\Phi}{dt}\right)$$

where $\Phi \equiv gz$ is the geopotential height and g the acceleration due to gravity, so that the vertical momentum equation can be written as:

$$\frac{\partial \Phi}{\partial p} = -\frac{RT}{p(1+\epsilon)}\,. \qquad (2.1)$$

Equation (2.1) (R is the gas constant for dry air, T the temperature, and p the pressure) establishes a relation between the height and pressure and is used for the coordinate transformation. This relation also implies that the nonhydrostatic system is feasible in p coordinates as long as $|\epsilon| < 1$ so that pressure remains a monotonic function of height in spite of the nonhydrostatic contributions.

Miller and White (1984) presented a more rigorous derivation of the equation set in both pressure and σ coordinates. The derivation is based on a systematic scaling and power series expansion in a parameter that is the fractional change in the potential temperature of a reference atmosphere over a typical convective scale depth. The assumption that this parameter is small ($\ll 1$) is nearly always valid in the troposphere. The approximate nonhydrostatic equation set is obtained as the zero-order balance of the original equations expanded in this small parameter. For a frictionless, adiabatic atmosphere without Coriolis force, the σ-coordinate equations in two dimensions are

$$\frac{du}{dt} = -\frac{\partial \Phi'}{\partial x} + \frac{\sigma}{p_*}\frac{\partial p_*}{\partial x}\frac{\partial \Phi'}{\partial \sigma} \qquad (2.2)$$

$$\frac{d\tilde{w}}{dt} = \frac{g}{RT_s}\frac{p}{p_*}\frac{\partial \Phi'}{\partial \sigma} + g\frac{\theta'}{\theta_s} \qquad (2.3)$$

$$\frac{d\ln p_*}{dt} + \frac{\partial u}{\partial x} + \frac{\partial \dot{\sigma}}{\partial \sigma} = 0 \qquad (2.4)$$

$$\frac{d\theta'}{dt} = -\frac{\theta_s}{g}N_s^2\,\tilde{w} \qquad (2.5)$$

$$\tilde{w} \equiv -\left(p_*\dot{\sigma} + \sigma\frac{dp_*}{dt}\right)\frac{RT_s}{gp} \qquad (2.6)$$

where

$$N_s^2 = -\frac{gp}{RT_s}\frac{g}{\theta_s}\frac{\partial \theta_s}{\partial p}$$

is the static stability of the reference atmosphere.

The above equations are, respectively, those for the horizontal and vertical momentum, mass continuity, and entropy conservation. Equation (2.6) is a definition of the vertical momentum in the σ coordinates. The vertical coordinate σ is defined as

$$\sigma \equiv \frac{p - p_t}{p_{\text{surf}} - p_t} = \frac{p - p_t}{p_*}$$

where p_{surf} is the surface pressure, p_t the constant pressure at the top boundary, and $p_* \equiv p_{\text{surf}} - p_t$. In the above equations, u is the x component of velocity, $\dot{\sigma} \equiv d\sigma/dt$ the vertical velocity in σ coordinates. The total derivative is defined as $d/dt \equiv \partial/\partial t + u\partial/\partial x + \dot{\sigma}\partial/\partial\sigma$; all the partial differentiations with respect to x and t are carried out at constant σ. The variable $\tilde{w}$ is the approximated vertical velocity that is shown by MW84 to contribute to the kinetic energy in a consistent manner.

In obtaining the above equations, the original equations are expanded around a reference state, which is similar to the way that the anelastic equation set is obtained (Ogura and Phillips 1962). Therefore

$$\Phi = \Phi_s(p) + \Phi'(x, \sigma, t)$$

$$\theta = \theta_s(p) + \theta'(x, \sigma, t), \qquad (2.7)$$

where Φ is the geopotential height and θ the potential temperature. Here "s" denotes the reference state, and the prime denotes the deviations. Potential temperature is defined as

$$\theta = T(p_0/p)^\kappa = T/\Pi \qquad (2.8)$$

where T is the temperature, $\Pi \equiv (p/p_0)^\kappa$ the Exner pressure, $\kappa \equiv R/C_p$ and R is the gas constant for dry air, C_p the specific heat of dry air at constant pressure, and $p_0 \equiv 1000$ hPa.

The reference state is required to be in a hydrostatic balance, therefore

$$\frac{d\Phi_s}{dp} = -\frac{R\theta_s}{p}\left(\frac{p}{p_0}\right)^\kappa. \qquad (2.9)$$

It should be noted that the reference state is not only a function of σ, it also depends on the horizontal coordinate x in the σ-coordinate system. To ensure the hydrostatic balance of the reference state, the following relations must be satisfied:

$$-\left(\frac{\partial \Phi_s}{\partial x}\right)_p = -\left(\frac{\partial \Phi_s}{\partial x}\right)_\sigma + \frac{\sigma}{p_*}\frac{\partial p_*}{\partial x}\frac{\partial \Phi_s}{\partial \sigma} = 0$$

$$\frac{\partial \Phi_s}{\partial \sigma} + \frac{RT_s p_*}{p} = 0 \qquad (2.10)$$

where $\Phi_s = \Phi_s(p) = \Phi_s(x, \sigma, t)$. These relations will be used later to determine Φ_s and Φ' at $\sigma = 1$, which are required as the lower boundary conditions for the elliptic equation for Φ'. The Φ' equation is obtained by applying the divergence operator on the momentum equations and is formally expressed as

$$E(\Phi') = F, \qquad (2.11)$$

its detailed form will be given later.

In the above system, there are five independent equations, Eqs. (2.2)–(2.6), but six variables, u, $\tilde{w}$, $\dot{\sigma}$, θ, Φ', and p_*. Since p_* is a boundary variable, a relation is obtained from the continuity equation using boundary conditions $\dot{\sigma} = 0$ at $\sigma = 0$ and 1 so that

$$\frac{\partial p_*}{\partial t} = -\int_0^1 \frac{\partial p_* u}{\partial x}\, d\sigma. \qquad (2.12)$$

Equation (2.12) states that the surface pressure variation results from the mass convergence/divergence in the column directly above, the direct nonhydrostatic contribution is neglected. The nonhydrostatic contribution to the mass continuity is of higher order according to MW84's scaling analysis, and its neglect is justified.

Without extra sources or sinks, or with these terms being known, Eqs. (2.2)–(2.3), (2.5)–(2.6), and (2.11)–(2.12) constitute a closed system. There are two ways to solve it: one solves the continuity Eq. (2.4) explicitly for the vertical motion without integrating vertical momentum Eq. (2.3); the other directly solves the vertical momentum equation with the mass continuity being implicitly ensured by Eq. (2.11). The former procedure is in line with that used in hydrostatic models, while the latter treats the horizontal and vertical components of momentum in a more consistent way and is similar to the way other nonhydrostatic equation systems are solved (e.g., Clark 1977). We use the later approach. The general procedure of time integration is: first predict u, w, θ', and p_* from Eqs. (2.2), (2.3), (2.5), and (2.12), then calculate $\dot{\sigma}$ from Eq. (2.6) and finally diagnose Φ' from elliptic Eq. (2.11).

b. Some properties of the equation system

MW84 showed that the σ-coordinate nonhydrostatic equation system is dynamically consistent in terms of energy conservation. The equation for the total energy is:

$$\frac{\partial (p_* E)}{\partial t} = -\left[\frac{\partial p_* u(E + \Phi)}{\partial x} + \frac{\partial p_* \dot{\sigma}(E + \Phi)}{\partial \sigma}\right] - \frac{\partial \sigma \Phi}{\partial \sigma}\frac{\partial p_*}{\partial t} \qquad (2.13)$$

with the total energy defined as

$$E \equiv \frac{1}{2}(u^2 + \tilde{w}^2) + C_p T.$$

An energy budget within a given domain can be obtained by integrating Eq. (2.13) over this domain, which will show that the change in the total energy is a result of energy fluxes through the lateral boundaries and the work done to the domain atmosphere by the ground surface forcing.

Miller (1974) and MW84 also performed a detailed linear analysis on the QNH equation system. It is found that vertically propagating sound waves are not supported in either the p-coordinate or the σ-coordinate system. The structure and phase speed of internal gravity waves are accurately represented. Lamb waves, i.e., the horizontally propagating sound waves, can be eliminated by imposing appropriate boundary conditions such as $\dot{\sigma} = 0$ at $p = p_{\text{top}} < 0$ in the σ-coordinate system.

3. The numerical formulation of the model

a. Model equations and finite differencing

The equation set given in the last section is extended to include diabatic and frictional processes and Coriolis effect. It includes three water categories, i.e., the water vapor, cloud water, and rain water. The conservation equations for them are coupled together through Kesler's (1969) microphysics parameterizations. The model described here is two-dimensional (independent of y) for simplicity, the extension into the third dimension is straightforward.

The Arakawa C grid is used in the model. This grid has a good representation of inertial gravity waves, and the variable arrangement facilitates conservative schemes for the advection terms. On a C-grid cell, state variables θ', Φ', and q_i (q_i stands for the specific content of water vapor, cloud water, or rain water) are defined at the cell center and the normal velocity components are defined on the corresponding sides.

The second-order centered-difference scheme is used for all spatial finite differencing, except when the flux-corrected transport (FCT) scheme (Zalesak 1979) is used to advect scalar quantities. Since implicit or semi-implicit time integration techniques used in hydrostatic σ-coordinates system (e.g., Hoskins and Simmons 1975) are not practical for the current equation system, the explicit leapfrog time integration scheme is used with respect to all processes except for the diffusion terms, which are evaluated one time step earlier to result in a forward scheme in time.

Adopting the notation of Shuman (1962), the full set of model equations in finite-difference form [except Eq. (3.10)] is as follows:

$$\begin{aligned}\delta_t\overline{(\overline{p_*}^{x}u)}^{t} = {}& -\mathrm{UFLUX}^{n} - \overline{p_*}^{x}\delta_x\Phi' \\ & + \sigma\delta_x p_*\delta_\sigma\overline{\Phi'}^{x\sigma} + \overline{p_*}^{x}(D_u{}^{n-1} + f\overline{v}^{x}) \qquad (3.1)\end{aligned}$$

$$\delta_t\overline{(p_*v)}^{t} = -\mathrm{VFLUX}^{n} - p_*f\overline{u}^{x} + p_*D_v{}^{n-1} \qquad (3.2)$$

$$\begin{aligned}\delta_t\overline{(p_*w)}^{t} = {}& -\mathrm{WFLUX}^{n} + p_*\overline{S}^{\sigma}\delta_\sigma\Phi' \\ & + p_*g\left[\overline{\left(\frac{\theta'}{\theta_s}\right)}^{\sigma} + 0.61\overline{q_v'}^{\sigma} - \overline{q_c}^{\sigma} - \overline{q_r}^{\sigma}\right] + p_*D_w{}^{n-1} \\ & \qquad (3.3)\end{aligned}$$

$$\begin{aligned}\delta_t\overline{(p_*\theta')}^{t} = {}& -\mathrm{TFLUX}^{n} - p_*\theta_sN_s{}^2\overline{w}^{\sigma}/g \\ & + p_*M_\theta{}^{n} + p_*D_\theta{}^{n-1} + p_*\dot{Q}/(C_p\Pi) \qquad (3.4)\end{aligned}$$

$$\delta_t\overline{p}_*^{t} = -\sum_j \delta_x(\overline{p}_*^{x}u)\Delta\sigma \qquad (3.5)$$

$$\begin{aligned}\delta_t\overline{(p_*q_i)}^{t} = {}& -\mathrm{QFLUX}^{n} + p_*(M_{q_i}^{n} + D_{q_i}^{n}) \\ & \qquad (3.6),\ (3.7),\ \text{and}\ (3.8)\end{aligned}$$

$$\dot\sigma = -Sw - \frac{\sigma}{p_*}\left[\overline{u}^{x\sigma}\delta_xp_* - \sum_j \delta_x(\overline{p}_*^{x}u)\Delta\sigma\right] \qquad (3.9)$$

$$\begin{aligned}&\frac{\partial^2\Phi'}{\partial x^2} - \frac{2\sigma}{p_*}\frac{\partial p_*}{\partial x}\frac{\partial^2\Phi'}{\partial x\partial\sigma} + \frac{\partial}{\partial\sigma}\left(S^2\frac{\partial\Phi'}{\partial\sigma}\right) \\ &\quad + \left(\frac{\partial \ln p_*}{\partial x}\right)^2\frac{\partial}{\partial\sigma}\left(\sigma^2\frac{\partial\Phi'}{\partial\sigma}\right) - \frac{\sigma}{p_*}\frac{\partial^2p_*}{\partial x^2}\frac{\partial\Phi'}{\partial\sigma} = F_\Phi. \\ &\qquad (3.10)\end{aligned}$$

The above system includes the effects of diffusion, diabatic heating, and earth rotation. There are three additional equations for the conservation of water vapor (q_v), cloud water (q_c), and rain water (q_r). Here D_ψ (ψ denotes θ' or q_i) represents subgrid-scale mixing and/or numerical diffusion, which can be referred to as diffusion in general. Term M_ψ represents the moisture and cloud microphysical processes that are given by the Kessler-type parameterizations, their detailed formulations are not given here. Term $\dot{Q}$ represents heat source or sink. The "tilde" in $\tilde{w}$ is omitted here and in the rest of this paper for convenience. The third term on the right-hand side of Eq. (3.3) is the full buoyancy in the presence of water-vapor and liquid-water loading. In Eqs. (3.5) and (3.9) the summation is done through the u levels between the top and bottom model boundaries.

The conservation equations are all formulated in flux form. For u and w, the advection (flux) terms are

$$\begin{aligned}\mathrm{UFLUX}^{n} &= \delta_x(\overline{\overline{p}_*^{x}u}^{x}\,\overline{u}^{x}) + \delta_\sigma(\overline{\dot\sigma p_*}^{x}\,\overline{u}^{\sigma}) \\ \mathrm{WFLUX}^{n} &= \delta_x(\overline{p_*}^{x}\,\overline{u}^{\sigma}\,\overline{w}^{x}) + \delta_\sigma(p_*\overline{\dot\sigma}^{\sigma}\,\overline{w}^{\sigma}); \qquad (3.11)\end{aligned}$$

for v, θ', and q_i they are written in a general form:

$$\mathrm{QFLUX}^{n} = \delta_x(\overline{p}_*^{x}u\overline{q}^{x}) + \delta_\sigma(p_*\dot\sigma\overline{q}^{\sigma}). \qquad (3.12)$$

In the above, the second-order centered-difference scheme is used. The advection terms thus formulated conserve the first and second moment of the quantity being advected (Lilly 1964; Arakawa and Lamb 1977). The kinetic energy and the potential temperature variance are therefore conserved in the advective processes, which ensures that nonlinear computational instability is effectively suppressed. When the flux-corrected transport scheme is used, QFLUX^{n} then represents the fluxes corrected in such a way as to eliminate the short wavelength numerical oscillations associated with high-order schemes, the positivity of the advected water quantities is then strictly maintained.

Equation (3.9) is a relation used to calculate $\dot\sigma$. Equation (3.10) corresponds to Eq. (2.11) and is an elliptic diagnostic equation for the geopotential height perturbation Φ'. It is obtained by performing divergence operation $\partial/\partial x(3.1) + \partial/\partial\sigma[-S(3.3)]$ where $S \equiv gp/(RT_sp_*)$ is a parameter having a dimension of inverse scale height. Here only the differential form of the Φ' equation is given and its finite differencing is straightforward. The right-hand side of this equation is given in the appendix.

The time integration procedure is explicit; Eqs. (3.1)–(3.8) are first integrated forward one time step for p_*, u, v, w, θ', and q_i; $\dot\sigma$ and Φ' are then diagnosed from Eqs. (3.9) and (3.10). The condensation and microphysics processes are incorporated in an adjustment step. Since the reference state defined on the σ levels is dependent on the pressure, in principle it needs to be updated every time step. However, experiments show that one update every a few time steps is sufficient.

The Robert–Asselin time filter (Robert 1966; Asselin 1972) is used to suppress the computational mode associated with the leapfrog scheme. A coefficient of 0.01 is used and the filter is applied at every time step to variables explicitly predicted by this scheme. The leapfrog scheme is stable under the well known Courant–Friedrichs–Lewy (CFL) condition. The removal of vertical sound waves in the current system greatly alleviates the restriction on time steps, especially when high vertical resolution is required.

b. Boundary conditions

At the lateral boundary, the radiative boundary condition (RBC) due to Orlanski (1976) is applied, in a way similar to Miller and Thorpe (1981), to the normal velocity component u, y-velocity v, potential temperature θ', and surface pressure p_*. It is also applied to the variables for water substance. The vertical velocity

$\dot{\sigma}$ at the boundary is calculated from the continuity equation. In some cases (when the domain size is small) it is necessary to adjust the normal velocity determined by the radiative boundary conditions to ensure the total mass conservation.

At the top and bottom boundaries the σ-coordinate vertical velocity $\dot{\sigma}$ vanishes by definition. The top boundary is a free surface where external gravity waves are supported but only long hydrostatic modes have fast propagation speed (Miller 1974). The bottom boundary is the ground surface $z = h(x)$. Free-slip boundary condition is assumed there, i.e., the normal gradient of tangential velocity vanishes. These conditions are expressed as $\dot{\sigma} = w = 0$ and $\partial u/\partial\sigma = 0$ at $\sigma = 0$, $\dot{\sigma} = 0$, $w = -dp_*/dt(p_*S)^{-1}$, and $\partial u/\partial\sigma = 0$ at $\sigma = 1$. At $\sigma = -\Delta\sigma$ and $\sigma = 1 + \Delta\sigma$, $\dot{\sigma}$ is diagnosed from the continuity equation and w is calculated according to its relation with $\dot{\sigma}$. This procedure will reduce to the mirror-type symmetry boundary condition if the pressure at the boundary is constant. Zero gradient condition is also assumed for θ and q_i at the top and bottom boundaries, but this is relevant only when calculating the cross-boundary turbulent fluxes.

c. *Solution of the elliptic diagnostic equation for Φ'*

As was pointed earlier, the elliptic diagnostic Eq. (3.10) is solved to obtain the geopotential height field. For a standard Poisson equation defined on a regular grid, many efficient direct solvers exist. However for more complicated elliptic equations such as Eq. (3.10), no general direct solver is available. Here the "block iteration" method is used, which combines a direct Poisson solver with the iteration technique. In Eq. (3.10) we move the terms that are relatively small [terms with coefficient proportional to $(1/p_*)(\partial p_*/\partial x)$] to the right-hand side and solve the resultant standard Poisson equation using a direct FFT solver. A sufficient accuracy can be achieved very quickly (depending on the relative variations in the surface pressure) after only a few iterations, each time with the terms on the right-hand side being updated using new values of Φ'. The details can be found in Xue (1989). In tests with dry convection, two iterations are sufficient on average without topography, a few more are otherwise required depending on the aspect ratio of orography slope.

At the lateral boundaries, Neumann boundary conditions are specified by calculating $\partial\Phi'/\partial x$ from the horizontal momentum equation [the differential form of Eq. (3.1)] applied at the lateral boundaries. The local time derivative of p_*u is given by the RBC. On the top boundary, $\sigma = 0$, the Neumann boundary condition is obtained by calculating $\partial\Phi'/\partial\sigma$ from the vertical momentum equation. The bottom of the model is a physical boundary, where the geopotential height is related to the surface topography $z = h(x)$:

$$\Phi|_{\sigma=1} = \Phi_s|_{p=p_{\rm surf}} + \Phi'|_{\sigma=1} = gh. \qquad (3.13)$$

Since the geopotential height of the reference state Φ_s is defined as a function of pressure p, its value at $\sigma = 1$ remains to be found. By combining the two relations in Eq. (2.10) and differentiating the resulting equation with respect to x at constant $\sigma = 1$, we obtain

$$\left.\frac{\partial^2\Phi_s}{\partial x^2}\right|_{\sigma=1} = -\frac{\partial}{\partial x}\left(\frac{RT_s}{p_{\rm surf}}\frac{\partial p_*}{\partial x}\right). \qquad (3.14)$$

The differentiation raises the order of the equation so that conditions of Φ_s at both $x = 0$ and $x = XL$ are used, this reduces the error accumulation when solving for Φ_s.

Assume for a reference atmosphere in a hydrostatic balance, the pressure is $p^0_{\rm surf}$ at $\Phi_s = gh$. To find Φ_s at $p_{\rm surf}$, we have from the hydrostatic relation

$$\Phi_s(p = p_{\rm surf}) = \Phi_s(p = p^0_{\rm surf}) - \int_{p^0_{\rm surf}}^{p_{\rm surf}} RT_s d(\ln p)$$

$$= gh + R\bar{T}_s \ln(p^0_{\rm surf}/p_{\rm surf}) \qquad (3.15)$$

where $\bar{T}_s$ is the average of T_s at $\sigma = 1$ and T_s of the reference atmosphere at $p^0_{\rm surf}$. Equation (3.15) is evaluated at boundaries $x = 0$ and $x = XL$ to obtain $\Phi_s(\sigma = 1, x = 0)$ $\Phi_s(\sigma = 1, x = XL)$, which serve as the boundary conditions for Eq. (3.14). The discrete approximation to Eq. (3.14) is a tridiagonal linear equation set and is solved directly. In three-dimensional cases the corresponding equation becomes a Poisson equation, which can also be directly solved. With Φ_s being known, Eq. (3.13) then gives the value of Φ' at $\sigma = 1$. This condition is crucially important in the model—it is this that relates the geopotential height at the surface to the surface pressure and therefore to the mass field in the interior.

Although Φ' at $\sigma = 1$ is known, the grid staggering requires Φ' at $\sigma = 1 + \Delta\sigma/2$ as the Dirichlet condition. To extrapolate Φ' to this level, $\partial\Phi'/\partial\sigma$ is derived from the vertical momentum equation. The local time tendency of w is not readily available, but the stability of the model solution is found to be very sensitive to its calculation. The model tests show it is best to omit this local tendency term, which is justified partly because its magnitude is small. Then the lower boundary condition for the Φ' equation is given by

$$\Phi'|_{\sigma=1+\Delta\sigma/2} = \Phi'|_{\sigma=1} + \frac{\Delta\sigma}{2}\left.\frac{\partial\Phi'}{\partial\sigma}\right|_{\sigma=1}. \qquad (3.16)$$

It should be noted that Φ' at the surface is directly related to $p_{\rm surf}$, therefore the nonhydrostatic contribution is not present there. On the other hand, the numerical model thus formulated produces accurate mountain flow solutions. The numerical simulations of squall lines where the propagation of the cold outflow strongly depends on the surface pressure also produce consistent results (Xue 1989). This approximation is therefore justified at least for the cases considered here.

At the early stage of model development, attempts were made to apply the normal gradient-type condition at the lower boundary. This practice results in a decoupling between the geopotential height at the surface and the interior mass field, the solution obtained is physically inconsistent and mostly unstable.

d. Subgrid-scale mixing and numerical diffusion

Smagorinsky (1963) suggested a formulation of subgrid-scale mixing for use in a general circulation model that depends on the magnitude of deformation tensor and the grid spacing. This formulation is extended by Lilly (1962) to include the contribution of convective available potential energy through the dependency on Richardson number, and it has since been widely used (e.g., Clark 1977; Durran and Klemp 1983, DK83 hereafter). The mixing coefficient for momentum is

$$K_m = (k\Delta)^2|\mathrm{Def}|[\max(1 - \mathrm{Ri}/\mathrm{Pr}, 0)]^{1/2} \qquad (3.17)$$

where $|\mathrm{Def}|$ is the magnitude of deformation and Ri the Richardson number. Here $\mathrm{Pr} = K_m/K_H$ is the turbulence Prandtl number whose value is to be determined for particular experiment, $k = 0.21$ after Deardorff (1971) and $\Delta = (\Delta x \Delta z)^{1/2}$.

In our model the mixing formulas are transformed into (x, σ) coordinates based on

$$\left(\frac{\partial\psi}{\partial x}\right)_{z=\mathrm{const}} \approx \left(\frac{\partial\psi}{\partial x}\right)_{\sigma=\mathrm{const}} - \frac{\sigma}{p_*}\frac{\partial p_*}{\partial x}\frac{\partial\psi}{\partial\sigma}$$

$$\frac{\partial\psi}{\partial z} \approx -S\frac{\partial\psi}{\partial\sigma} \qquad (3.18)$$

where ψ is any dependent variable. The approximations in the transformation are consistent with those made to obtain the nonhydrostatic system. The mixing terms are finite differenced using centered differencing.

In practice, a constant numerical diffusion is necessary to remove numerical noise. Since diffusion on the full variables tends to destroy the nonconstant fields of the initial or reference state, the background diffusion is formulated so that it operates only on the perturbations from the base state.

An absorbing layer with enhanced damping is included near the top boundary to simulate a radiative top boundary condition. Two options of damping are available, one is the viscous type of damping and the other the Rayleigh damping. The damping is applied to the perturbation variables and incorporated to the right-hand side of the equations for u, v, w, θ', and q_i. The damping coefficient profile of the cosine-squared form is specified after Klemp and Lilly (1978), which increases smoothly from a certain height to the model top. Klemp and Lilly (1978) suggested that, for linear hydrostatic waves, the minimum depth of the absorbing layer is approximately one vertical wavenumber. In this σ-coordinate model the vertical levels are stretched with height, an absorbing layer of a given depth therefore contains fewer levels so that the use of the absorbing technique is relatively economic. In this aspect, the applicability of the radiative upper boundary condition of Klemp and Durran (1983, KD83 hereafter) to the current model is worth exploring.

4. Model experiments with dry flows over a mountain ridge

In this section the numerical model is verified against linear and nonlinear analytical solutions of 2D flows over a bell-shaped mountain. The model is later used to simulate the 11 January, 1972 Boulder severe downslope windstorm and the results are compared with those of previous studies. The comparison establishes the credibility of the model in large-amplitude nonlinear wave regimes and the simulation demonstrates the development mechanism of the severe downslope winds in the Boulder event.

a. Mountain gravity waves in a uniform flow

Linear analyses on mountain gravity waves have been done by many authors and excellent reviews have been given by Alaka (1960) and Smith (1979). In an anelastic, uniformly stratified (N^2 = const), constant ($\bar{U}$ = const) rotational flow in x and z plane, steady-state gravity waves have the dispersion relation:

$$m^2 = [(k_s^2 - k^2)k^2 + \Gamma^2 k_f^2]/(k^2 - k_f^2) \qquad (4.1)$$

where k and m are the horizontal and vertical wavenumber, respectively, $k_s = l = (N^2/\bar{U}^2 - \Gamma^2)^{1/2}$ is the Scorer parameter, which represents the intrinsic vertical scale of a given flow and determines whether a particular wave mode can propagate in the vertical ($\Gamma \equiv \frac{1}{2} d\ln\bar{\rho}/dz$ is a stratification parameter that vanishes for a Boussinesq flow); and $k_f = f/\bar{U}$ gives the inertial scale of the flow. Consider a bell-shaped mountain profile $h(x) = h_m/(1 + x^2/a^2)$, the dominant horizontal wavenumber forced by the ridge is $k_0 = 1/a$. Using typical values of k_s (10^{-3} m^{-1}) and k_f (10^{-5} m^{-1}), Queney (1948) exemplified the wave solutions in different regimes depending on the horizontal scale of the mountain.

In the case where $a \sim 1/l$, i.e., $k_0 \sim k_s$, the mountain scale is comparable to the intrinsic vertical scale of the flow and the solution is nonhydrostatic. This solution is characterized by the "trailing waves" at the upper levels to the lee of the mountain. The wave energy propagates upwards from the mountain source and disperses downstream. When $a \gg 1/l$ the flow becomes hydrostatic, the waves become nondispersive in the horizontal and propagate only in the vertical. For a very broad mountain with $a \sim \bar{U}/f$. i.e., $k_0 \sim k_f \ll k_s$, the waves are hydrostatic and rotational and are dispersive in the horizontal due to rotational effects. The wave patterns for these three regimes are shown respectively in Figs. 1, 2, and 3 of Queney (1948).

The model solutions of mountain waves over a bell-shaped mountain of different horizontal scales are presented in the following. These waves are respectively in the nonhydrostatic, hydrostatic irrotational, and hydrostatic rotational regime. The atmosphere is assumed isothermal with $T_s = 250$ K, and the basic flow has a constant speed $\bar{U} = 20$ m s^{-1}. As a result, $N^2 = g^2/(C_p\bar{T})$, $\Gamma = g/(2R\bar{T})$ are both constant and the Scorer parameter $l = 0.977 \times 10^{-3}$ m^{-1}. Unlike in the solution shown in Queney (1948), the Boussinesq approximation is not assumed, i.e., the vertical density variation is retained in the model solutions. This will only modify the amplitude of the waves but not the wave structure for a given constant Scorer parameter. The model solutions can still be qualitatively compared with Queney's solutions when the mountain height is small. The parameters of model experiments are listed in Table 1 in which NX and NS are the number of grid points in x and σ direction, respectively. In the first three experiments, mountain height is small ($h_m/a \ll 1$) so that the waves are essentially linear and the results can be verified against linear analytical solutions.

The reference atmosphere is assumed to be in a balanced state. In this σ-coordinate model, the surface pressure, the pressure at the σ levels, and the state variables at these levels are interrelated, so that a procedure is needed to set up the initial state of the model. For the following experiments reference state temperature is specified as a function of height. To initialize the model, temperature is first given an initial guess on the model grid and iterations are performed based on the hydrostatic relation until a reasonable convergence is reached. A similar iterative step is taken in Anthes and Warner (1978) for a hydrostatic σ-coordinate model. The flow speed is initially specified as a function of height, the mountain is introduced at the beginning and flow is allowed to adjust to the presence of mountain.

The solutions for these experiments are smooth, the leapfrog-centered scheme is accurate enough so that FCT is not used for θ advection. The average surface pressure is 1000 hPa, and $p_{\text{top}} = 100$ hPa. The time steps listed in Table 1 are close to the maximum possible values under the CFL condition. It can be seen that the relation between Δt and Δx is not linear—Δt is relatively large for small Δx. For waves represented on C grid, $2\Delta x$ wave modes impose the strongest limitation on the time step (Haltiner and Williams 1980) and the largest possible time step for staggered C grid is half of that for nonstaggered grid. Table 1 suggests that the speed of fastest $2\Delta x$ waves is less than 100 m s^{-1} when $\Delta x = 0.4$ km, this significantly alleviates the restriction on the time step. When $\Delta x = 20.0$ km, even the shortest external waves become hydrostatic, whose speed is about 250 m s^{-1} so that a relatively small Δt has to be used.

The restriction by external gravity waves on the time step becomes serious when the horizontal grid length is of the order of 10 km. Fully implicit time integration is not practical for the given equation set, but the mode-splitting technique may be feasible. If implemented, the model efficiency would be improved a lot when Δx is of the order of 10 km. When Δx is of the order of 1 km the time step is already relatively large without mode-splitting.

Only a weak background diffusion is included in these experiments. A Rayleigh damping type absorbing layer occupies levels between 12 and 18 km. The e-folding time of damping at the top of this layer is respectively 1, 5, and 50 min for LMW1, LMW2, and LMW3. The w and θ fields from these experiments are shown in a nondimensionalized horizontal scale ($X = x/a$), at nondimensional time $T = t\bar{U}/a = 30$, when the solutions are nearly steady. The perturbations are scaled to correspond to the solutions over a 500-m height mountain ridge.

Figure 1 depicts the fields of w and θ for LMW1. These waves, being forced by a narrow ridge with 2-km half-width, exhibit clearly a trailing nonhydrostatic lee wave pattern at higher levels. The wave amplitude increases with height due to the decrease in air density. The airflow is displayed by the isentropes that are very close to the trajectories. The isentropes compare very closely to the streamlines shown in Queney's solution (Fig. 1 in Queney 1948). Figure 2 shows the solutions from LMW2. Given the breadth of the mountain, the waves are essentially nondispersive and hydrostatic. The waves are located directly over the ridge, the phase lines tilt upstream implying an upward wave energy propagation. The model solution displays a vertical wavelength of about 6.6 km, which is close to the predicted value $L_z = 2\pi/l \approx 6.45$ km. The flow pattern in Fig. 2b closely resembles the corresponding solution of Queney (1948).

In experiment LMW3 the mountain half-width is 100 km so that the mountain waves are hydrostatic

TABLE 1. Experiments of mountain waves in a uniform flow.

Experiment	Wave regime	Scale a (km)	h_m (m)	(NX, NS)	Δx (km)	Δt (s)	f(s^{-1})
LMW1	nonhydrostatic	2.0	1.0	(257, 41)	0.4	3.0	0.0
LMW2	hydrostatic, nonrotational	10.0	1.0	(129, 41)	2.0	8.0	0.0
LMW3	rotational, hydrostatic	100.0	10.0	(129, 41)	20.0	25.0	10^{-4}
NLMW2	nonhydrostatic	2.0	500.0	(257, 41)	0.4	3.0	0.0
NLMW2	hydrostatic, nonrotational	10.0	500.0	(129, 41)	2.0	8.0	0.0

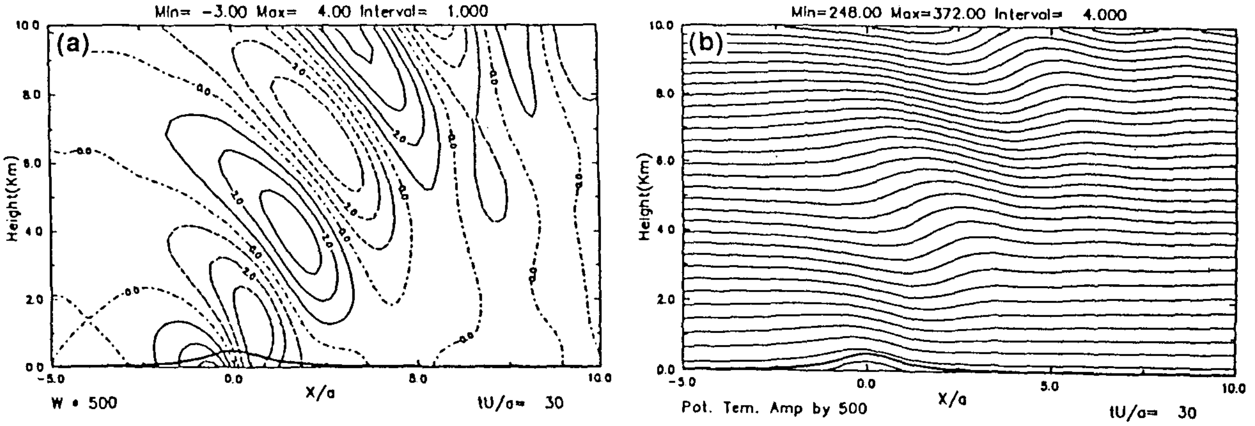

FIG. 1. The model solutions of (a) vertical velocity w and (b) isentropes (θ contours) from linear mountain wave experiment LMW1, at ND-time $T = 30$. Dimensional parameters in this run are $a = 2$ km, $U = 20$ m s^{-1}, and $N \approx 2 \times 10^{-2}$ s^{-1}, the flow is in the nonhydrostatic wave regime. The solutions are amplified to correspond to a solution over a 500-m mountain ridge.

and rotational. The w field in Fig. 3 shows the existence of a trailing wave train downstream of the mountain range due to the inertial effect. The horizontal wavelength of the inertial oscillations at the downstream surface is close to the prediction of $L_x = 2\pi\bar{U}/f \approx 1256$ km. The downstream dispersion of wave energy results in a decrease in the wave amplitude upwards despite the counter effect of density scaling. The wave pattern shown by the isentropes in Fig. 3b qualitatively agrees with that of the analytical solution of Queney (1948).

The vertical flux of horizontal momentum due to wave motion is defined as

$$M = \int_{\infty}^{-\infty} \rho u'w'dx. \qquad (4.2)$$

Eliassen and Palm (1960) showed that for linear steady mountain waves, M is constant with height except at levels where $\bar{U} = 0$. The pressure drag that the flow imposes on the mountain surface is

$$D = \int_{\infty}^{-\infty} \rho p(z = h)\frac{dh}{dx}dx \qquad (4.3)$$

and for small amplitude waves $M = -D$.

Miles and Huppert (1969) showed that for irrotational hydrostatic waves over a finite-amplitude bell-shaped mountain, the momentum flux is to the first approximation

$$M = -\frac{\pi}{4}\rho_0 N\bar{U}h_m^2\left[1 + \frac{7}{16}\left(\frac{h_m}{l}\right)^2\right]. \qquad (4.4)$$

When the mountain is sufficiently low, i.e, $h_m/l \ll 1$, the above formula reduces to that for linear mountain waves

$$M_H = -\frac{\pi}{4}\rho_0 N\bar{U}h_m^2 \qquad (4.5)$$

as is given in Eliassen and Palm (1960). Bretherton (1969) showed that among all the wave regimes the

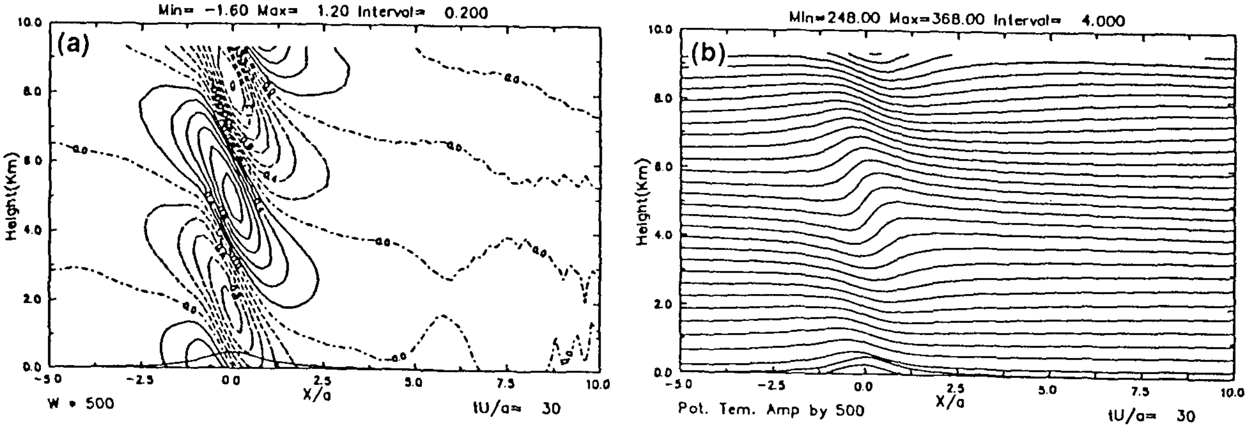

FIG. 2. As in Fig. 1 but are solutions from experiment LMW2. In this experiment, the mountain half-width is 10 km, so that the flow is in the hydrostatic irrotational wave regime.

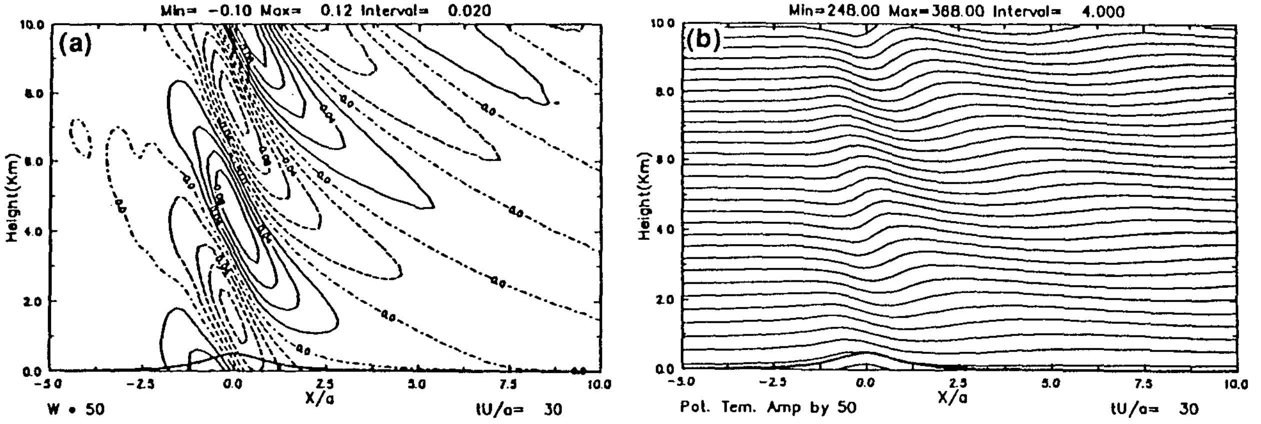

FIG. 3. As in Fig. 1 but are solutions from experiment LMW3. The mountain is broad in this case with a = 100 km, the waves are hydrostatic rotational.

hydrostatic irrotational mountain waves is most effective in transferring the horizontal momentum vertically.

The vertical flux of horizontal momentum is calculated according to Eq. (4.2) for experiment LMW1 and LMW2. The vertical profiles at various ND-time are shown in Fig. 4a for LMW1 and in Fig. 4b for LMW2. These fluxes are scaled by the analytical value for linear waves given by Eq. (4.5) (shown as the bold line in the figure). Figure 4b shows that for the hydrostatic waves in LMW2, the flux at higher levels gradually converges towards the analytical value with time and reaches 95% at the height of one vertical wavelength (~6.4 km) by T = 40. A similar convergence rate and accuracy were reported by DK83 in their tests with a compressible mountain wave model. The flux at lower levels is within 99% of the analytical value. A time dependent evolution of the momentum profiles is given analytically by Klemp and Lilly (1980), which have similar shapes to our profiles except the model solution develops somewhat more slowly. The profiles of momentum flux for the nonhydrostatic waves in LMW1 (Fig. 4a) show a similar convergence rate, but the magnitude is about 0.8 of the hydrostatic flux. This agrees with analytical prediction well (see, e.g., Fig. 3 of KD83 for $Na/U = 2$).

If the vertical acceleration term is dropped from the vertical momentum equation, the equation set reduces to the usual hydrostatic system and can then be solved in a standard way (e.g., as in Anthes and Warner 1978).

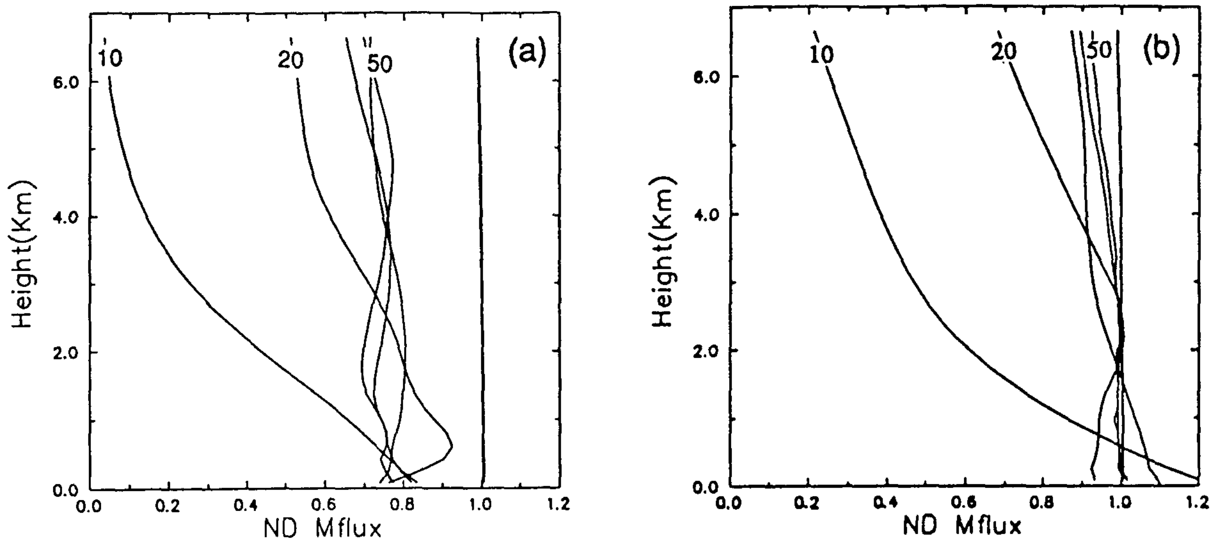

FIG. 4. The profiles of the vertical flux of horizontal momentum transported by (a) nonhydrostatic mountain waves in experiment LMW1 and (b) hydrostatic waves in LMW2, at ND-time T = 10 through 50. The fluxes are normalized by the analytical flux for linear hydrostatic waves, which is shown in bold line.

Φ' is obtained from the hydrostatic relation and $\dot{\sigma}$ is diagnosed from the continuity equation. A 3-s time step is required for a hydrostatic model version run of LMW2, this is because now the shortest external gravity waves are hydrostatic. The solution appears essentially the same as that from LMW2. However, when the hydrostatic version of the model is used to solve for wave solution over a narrow ridge ($a = 2$ km) as in LMW1, the obtained waves are rendered hydrostatic so that they are similar to those in LMW2 instead of those in LMW1. Figure 5 shows the profiles of vertical flux of momentum in this experiment, the magnitude of flux is now very close to the hydrostatic value. Clearly the nonhydrostatic nature of waves on this scale is completely distorted.

All the foregoing experiments are nearly linear, which constitute only a weak test on the model in terms of the lower boundary forcing. The comparison of the nonlinear model solutions with known analytical solutions would be a more rigorous test. Long (1953) showed that for constant mean flow speed and static stability, the steady-state equation of motion become linear with nonlinear boundary conditions and may be solved for vertically propagating waves (e.g., Lilly and Klemp 1979; Laprise and Peltier 1989c). Since our model does not make the Boussinesq approximation, only qualitative comparison can be made with Long's solution; however, a quantitative comparison can be made of the vertical momentum fluxes.

NLMW1 and NLMW2 are two experiments corresponding to LMW1 and LMW2, except that the mountains are of finite amplitude. Figures 6 and 7 show the solution from NLMW1 and NLMW2, respectively, for a 500-m height ridge. In both cases, the wave magnitude is larger than that obtained by amplifying linear solutions (see Figs. 1 and 2). This is consistent with the analytical result that linear boundary condition underestimates the true mountain height (Lilly and Klemp 1979).

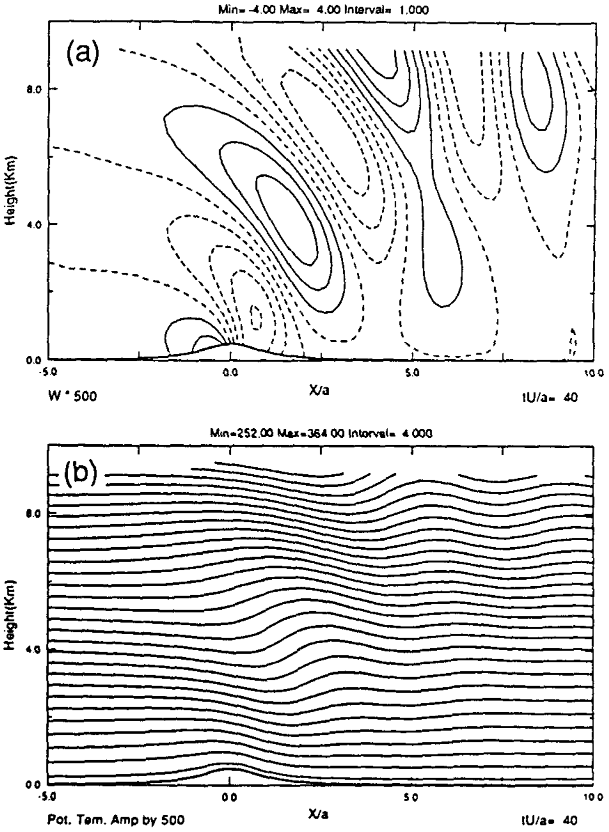

FIG. 6. As in Fig. 1 but are solutions from NLMW1, in which the mountain is of finite amplitude (500 m). The files are shown at $T = 40$, since the initial flow is set up over a $T = 5$ time period. The isentrope field shows that the flow near the lower boundary is better treated in this true nonlinear run.

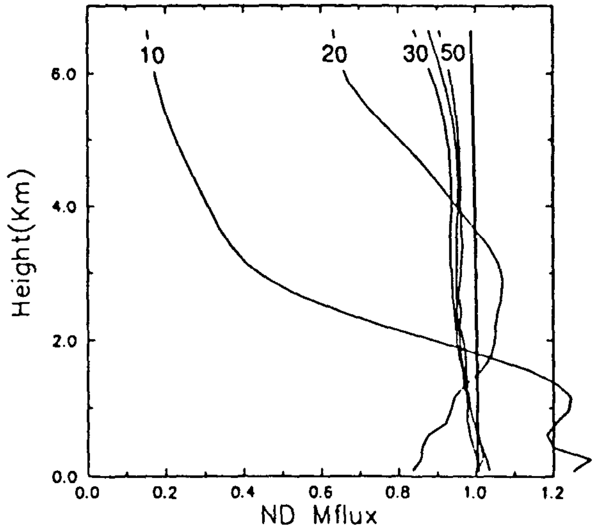

FIG. 5. The profiles of the vertical flux of horizontal momentum transferred by the mountain waves over a narrow ridge ($a = 2$ km) as in LMW1 but obtained using the hydrostatic version of the numerical model. The flux profiles appear very similar to those in LMW2 instead of LMW1, the nonhydrostatic effects are lost.

The momentum flux transported by nonlinear mountain waves, as given in Eq. (4.4), is a factor of $1 + 7/16(h_m/l)^2$ greater than the linear value. For NLMW2, this factor is approximately 1.1. Figure 8b shows the profiles of vertical momentum fluxes from NLMW2, as scaled by the linear hydrostatic value given in Eq. (4.5). The fluxes are obtained by first interpolating the local flux to a constant height level then integrating horizontally according to Eq. (4.2). In NLMW1 and NLMW2, the flow is gradually accelerated to its full speed over a period of $T = 5$ since the shock model startup used earlier tends to produce high-frequency oscillations initially in the surface pressure drag. The profiles of momentum flux for these two cases are shown in Fig. 8. Figure 8b shows that the flux in NLMW2 overshoots at the low levels at around $T = 10$ (the maximum is at $T \approx 9$), which may be attributed to the initiating procedure. By $T = 20$ the

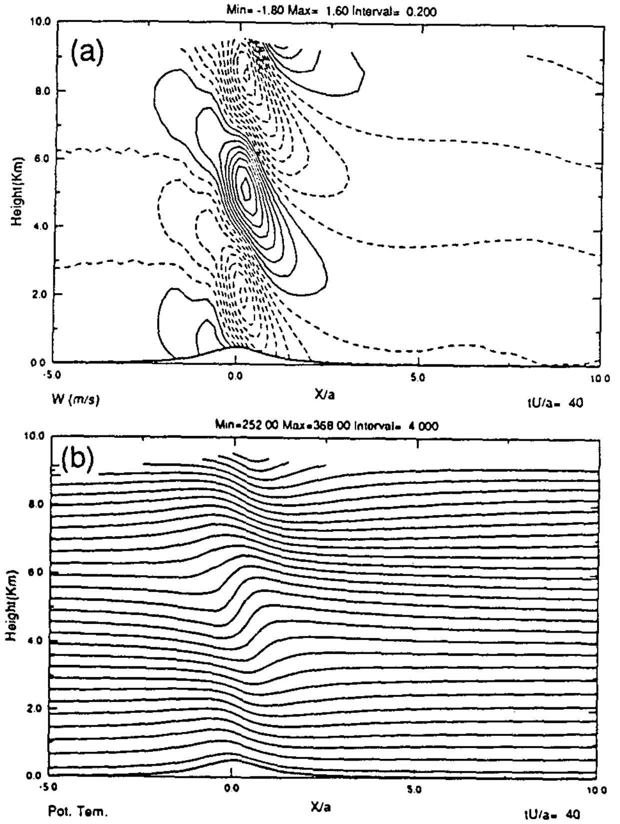

FIG. 7. As in Fig. 2 but are solutions from NLMW2, in which the mountain is of finite amplitude (500 m). The fields are shown at $T = 40$ as in Fig. 6.

magnitude of the flux is close to 1.1 over the one wavelength depth. The flux is roughly constant with height at later times, but a tendency to drift away from the predicted 1.1 is seen from $T = 50$. The trend of drifting is dependent on the height of absorbing layer and is believed to be related to the imperfect radiative upper boundary conditions. A similar phenomenon of drifting was also found by KD83 when they were testing their radiative upper boundary condition. The profiles of momentum flux for nonlinear, nonhydrostatic waves in NLMW1 are shown in Fig. 8a. The flux is nearly constant with height after $T = 30$. Although there are oscillations in the magnitude of these fluxes, overall they are higher than the linear values (c.f. Fig. 4a) but lower than the corresponding hydrostatic ones.

We conclude therefore that in the experiments with dry mountain waves over a mountain ridge of different heights and horizontal scales, the model using new nonhydrostatic σ-coordinate equations is successful in producing reasonably accurate solutions.

b. Simulation of the 11 January 1972 Boulder severe downslope windstorm

Severe downslope windstorm has been subject to extensive studies in recent literature, especially after the well-documented event of 11 January 1972 that occurred over the Continental Divide of the Rocky Range (Lilly and Zipser 1972; Lilly 1978). On that day Boulder Colorado experienced one of its most severe downslope windstorms with surface winds gusting as high as 55 m s^{-1}.

Many studies have been carried out on this particular event. An early study of Klemp and Lilly (1975) based on linear analyses showed that the vertical structure of the atmosphere has a strong influence on the wave amplitude on the lee slope. A strong wind was obtained

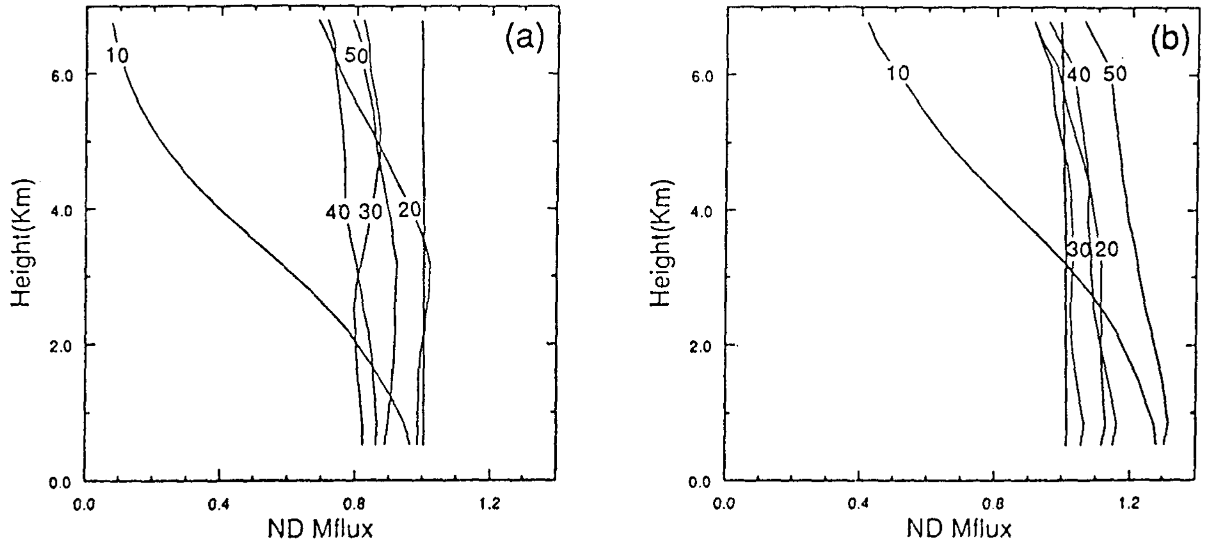

FIG. 8. The profiles of the vertical flux of horizontal momentum transported by finite amplitude (a) nonhydrostatic mountain waves in experiment NLMW1 and (b) hydrostatic waves in NLMW2, at ND-time 10 through 50. The fluxes are normalized by the analytical flux for linear hydrostatic waves. The fluxes are higher than the corresponding linear model results shown in Fig. 4.

in a nonlinear numerical simulation of the Boulder event in Klemp and Lilly (1978) using an isentropic coordinate model. Peltier and Clark (1979, PC79 hereafter) studied the same event using a 2D nonhydrostatic numerical model in terrain-following z coordinates and obtained a state that appeared very close to the observed one. In this case strong downslope winds develop after the topographically forced waves break near the tropopause, after this time, the surface pressure drag increases rapidly. Based on linear concept, PC79 proposed a mechanism that leads to the amplification after wavebreaking—the well-mixed region of wavebreaking is to act as a self-induced critical level that reflects waves incident onto it from below, forming a cavity between it and the ground in which wave disturbances amplify by wave resonance. Peltier and Clark (1983) showed for uniform flow and constant stratification case that wave energy is indeed confined to levels below the wave breaking region. The mechanism of PC79 is further supported by most recent studies of Laprise and Peltier (1989a, 1989b, LP89a,b hereafter). A stability analysis of the nonlinear steady state solution to Long's model is carried out (LP89a). An unstable deep resonant mode is found that is trapped in the cavity between the ground and the level of maximum streamline overturning; this mode extracts its energy from the mean sheared flow. This finding is also confirmed by the transient analysis of nonlinear solutions of numerical model (LP89b). Therefore, at least initially this unstable mode is responsible for the wave amplification below the wave breaking layer that leads to the onset of strong downslope winds.

Along a different line, Smith (1985) exploited the mechanism that views the severe downslope winds as an internal wave analogue of the hydraulic jump in a flow with a free surface over an obstacle. Under certain parameter setting, the steady-state solution to Long's equation is obtained, an assumed free surface between a stagnant well-mixed region and the flow underneath deflects downwards, and the flow undergoes a transition from a subcritical to a supercritical state. With a set of properly chosen parameters, the obtained transitional flow is qualitatively similar to the Boulder storm observation. Durran (1986) further exploited the hydraulic analogue in a continuously stratified flow and showed that the flow transition can occur in the presence of an interface between layers of different static stability. In the Boulder case, a stable layer at the low level is responsible for the initial low-level flow acceleration, which in turn forces the waves at the tropopause to break. After the wave breaking, an interface is created between the well-mixed neutral stability layer and the stable layer below, and this interface is analogous to the free surface of a hydraulic flow. With energy confined below this interface, the flow beneath undergoes a transition from a subcritical state to a supercritical state, producing strong wind on the lee slope. However, there are certain limitations in this theory—the theory itself does not predict the formation of the assumed interface, neither does it present a physical picture of the transition from an internal wave-dominated state to a state that resembles the hydraulic jump type of flow.

In the following a simulation the Boulder storm using our model is presented. The simulation is carried out for a longer time than those reported by previous authors (e.g., PC79; and Durran 1986), although most recently Scinocca and Peltier (1989, SP89 hereafter) also performed a series of extended period simulations. While the amplification after the wave breaking can be explained by PC79 and LP89a's resonant growth mechanism, the ultimate state of flow is very similar to that given by the hydraulic theory (Smith 1985), suggesting the validity of this theory in the fully nonlinear limit. The comparison with other model's simulations also serves as the model verification in the severe nonlinear regime.

The profiles of upstream potential temperature and wind speed are plotted in Fig. 9. The atmospheric structure has an unusually strong upper-tropospheric jet and a relatively weak static stability except in a shallow layer just above the mountain peak. Figure 9d shows, except in the shallow stable layer, a rapid decrease in the Scorer parameter from the ground level upwards to much smaller values above 4-km height. Short waves are therefore expected to be trapped at low levels to form lee waves. For longer hydrostatic mountain waves there will be a three-quarter wavelength phase shift across the depth of troposphere so that the first overturning of isentropes is expected to be at the tropopause (PC79).

The control simulation of the Boulder severe windstorm uses 193 points in horizontal with grid length $\Delta x = 1$ km, and 41 levels in the vertical with $p_{\text{surf}}(z = 0) = 850$ hPa and $p_{\text{top}} = 30$ hPa. The time step Δt is 4 s. Following previous investigators, a symmetric bell-shaped mountain ($h(x) = h_m/[1 + (x/a)^2]$) with half-width $a = 10$ km is used and is located at the center of the model domain. The mountain height h_m is 2 km. The top of the model domain is about 22 km above the ground level, from which a sponge layer extends down to 15-km height. Rayleigh type damping is employed, with the shortest e-folding time of damping being 5 min at the top of the domain. A full formulation of turbulence mixing with the deformation and Richardson number dependent mixing coefficients is used, and the eddy Prantl number $\text{Pr} = K_m/K_H = 1$ is assumed. A weak constant background diffusion is included to remove numerical noise and it operates only on the deviations from the initial state. A coefficient $K_{BG} = 200$ m^2 s^{-1} is used for the control run, with other values being used in sensitivity experiments where only slight changes in the timing of the wave development are found. On the lateral boundaries, the radiative conditions described in section 3 are used. The initial temperature and wind fields are only height

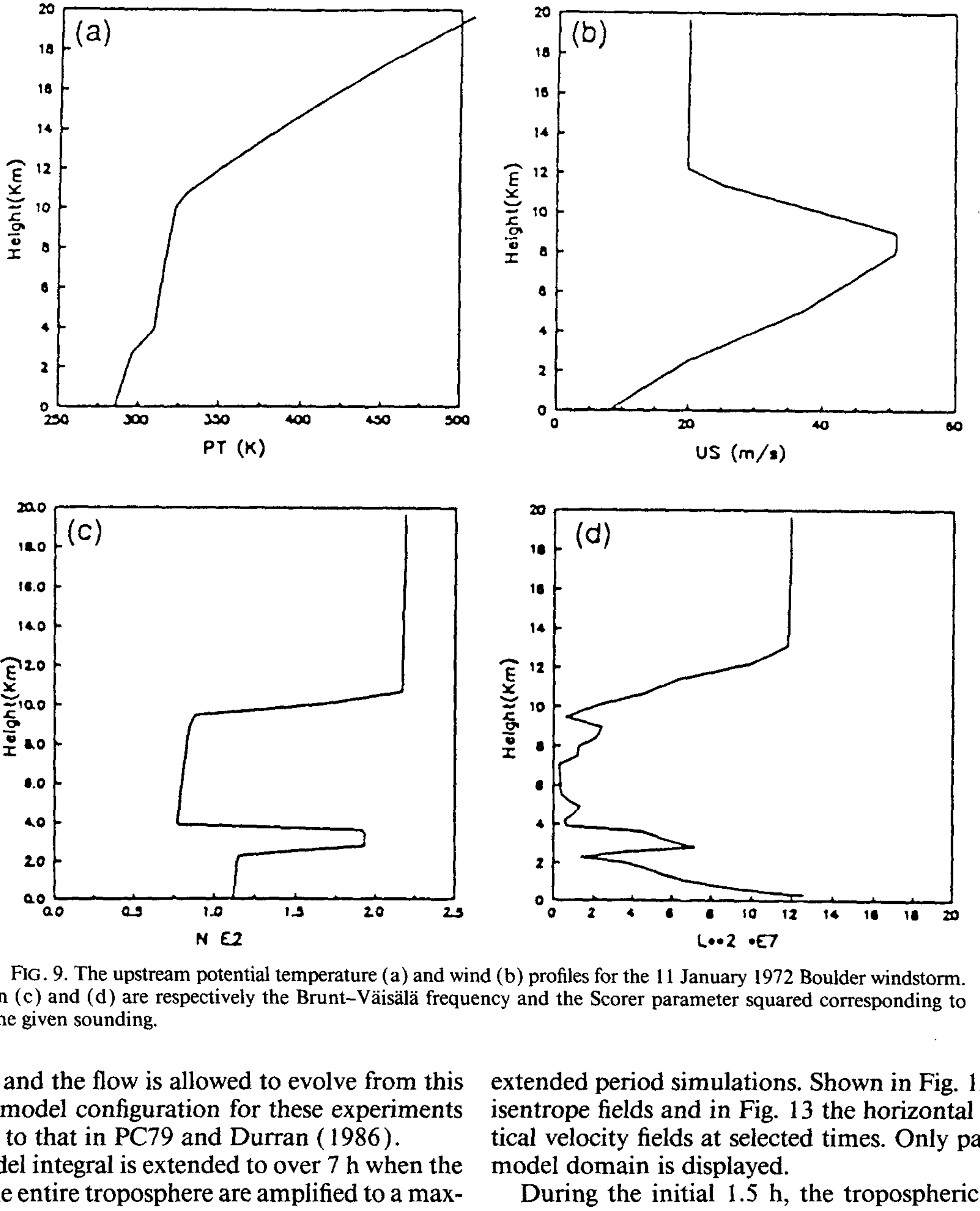

FIG. 9. The upstream potential temperature (a) and wind (b) profiles for the 11 January 1972 Boulder windstorm. In (c) and (d) are respectively the Brunt–Väisälä frequency and the Scorer parameter squared corresponding to the given sounding.

dependent and the flow is allowed to evolve from this state. Our model configuration for these experiments are similar to that in PC79 and Durran (1986).

The model integral is extended to over 7 h when the waves in the entire troposphere are amplified to a maximum intensity. The time evolution of the surface pressure drag as defined by Eq. (4.3) is plotted in Fig. 10, together with the linear analytical value shown in dashed line. The drag curve is smoothed in time therefore fast transients are removed. The time evolution of the surface pressure drag reported by PC79 (dashed line) and by DK83 (solid line) are reproduced in Fig. 11. It can be seen that the magnitude of drag obtained in these three different simulations agree fairly well within the early period when results are all available. During the period that follows, the surface drag triples again, becoming an order of magnitude greater than the linear prediction (3.8×10^6 kg s^{-2} versus 3.04×10^5 kg s^{-2}). A similar result is also found by SP89 in their extended period simulations. Shown in Fig. 12 are the isentrope fields and in Fig. 13 the horizontal and vertical velocity fields at selected times. Only part of the model domain is displayed.

During the initial 1.5 h, the tropospheric flow, in response to the presence of mountain ridge, develops a deep wave pattern that indicates isentrope overturning at the tropopause (Fig. 12b). The height of overturning level agrees well with the linear prediction of PC79. The low-level flow response is very strong even before the tropopause wavebreaking occurs and the surface wave drag is already three times that of linear prediction, nonlinearity clearly plays an important role even in this early stage. In our model simulation, the isentrope overturning is first seen at 1.5 h at the tropopause (figures not shown). As this occurs, the wave breaks and a well-mixed region of air is created that, as is argued in PC79, acts to reflect wave energy from below. LP89a showed the unstable resonant mode ex-

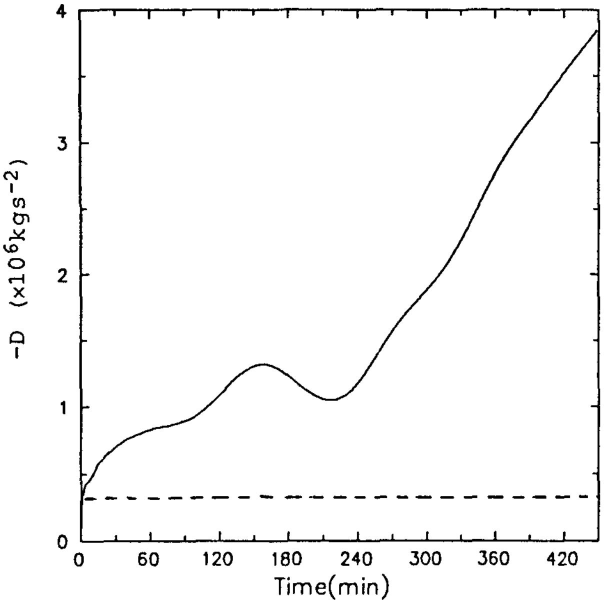

FIG. 10. The time evolution of surface pressure drag ($\times 10^6$ kg s^2) from the our model simulation of the Boulder windstorm.

isting between the ground, and the mixed layer is, at least immediately after the overturning, responsible for the downslope flow amplification. Our isentrope field at 2.5 h (Fig. 12c) is very similar to that at the ending time of PC79. After 2.5 h, the downslope flow continues to accelerate, while the flow originating at the tropopause deflects further downwards, forming a progressively larger well-mixed region (Fig. 12e,f). After this time when an interface between the well-mixed layer and the flow below is formed, the hydraulic theory can be invoked to explain the nonlinear behavior of the downslope flow. The downslope flow (Fig. 12b) is relatively weak at 2 h. This follows the onset of wave breaking and reflects the transition from a regime dominated by low-level flow acceleration into the one in which the entire tropospheric flow behaves like a hydraulic jump. The surface wave drag curve (Fig. 10) displays a dip near 4 h, and this may be caused by the onset of a secondary wave breaking at the tropopause (Fig. 12d). Relating to this breaking, secondary resonant mode forms and interacts with the primary one so as to change the resultant wave drag on the mountain surface. The secondary wave breaking is also evident in the simulation of SP89 (see Fig. 7c of the paper) though not as pronounced. This difference may be partly due to the reflection from the top boundary, however, changing the magnitude of damping and the height of the sponge layer did not show great sensitivity. Further tests may be needed that involve raising the height of the top boundary and increasing the resolution at the upper levels in this σ-coordinate model.

Figure 13 shows that the horizontal flow speed along the downslope is as high as 72 m s^{-1} at 7 h. Though it is higher than the observed value (55 m s^{-1}), it indicates the possibility of such a strong wind given the environmental condition. In the real situation, surface friction should have limited the maximum surface wind, and the upstream condition may not have been maintained long enough for the flow to fully develop. The final simulated flow pattern is very similar to the observed one (Lilly 1978). Compared with the simulations of earlier studies (e.g., PC79 and Durran 1986), the deep trapped wave modes to the lee of the mountain are more prominent in our solution, these modes are related to the successive wave breaking regions at the tropopause and are similar in nature to the resonant mode found by LP89a.

Given the current model configuration, our model simulation did not reach a final state of saturation as in SP89. To obtain such a final state, a large model domain of the order of 360 × 50 km^2 with a mesh size of 720 × 144 was found necessary by SP89. The very large horizontal domain was required to minimize the upstream influence, while in the vertical a deep smoothly changing absorbing layer was needed to minimize downward reflection. However, given the domain size used in the current simulation, the model is delivering a solution that is very realistic in comparison with both the observation and the results from other different types of models. This is a major point we intend to demonstrate here.

A number of sensitivity experiments were also carried out. They include increasing the spatial resolution, decreasing the integration time step, repositioning the lateral boundaries relative to the mountain, altering the top boundary pressure level and reducing the back-

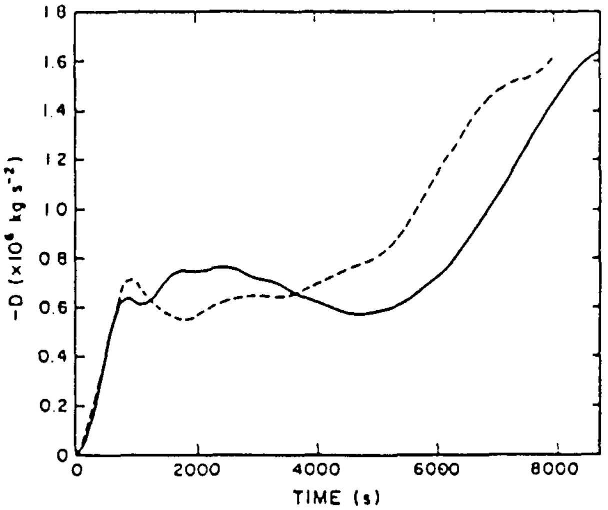

FIG. 11. The time evolution of surface pressure drag obtained by PC79 (dashed line) and by Durran and Klemp (1983) (solid line) in their simulations of the Boulder windstorm (reproduced from DK83).

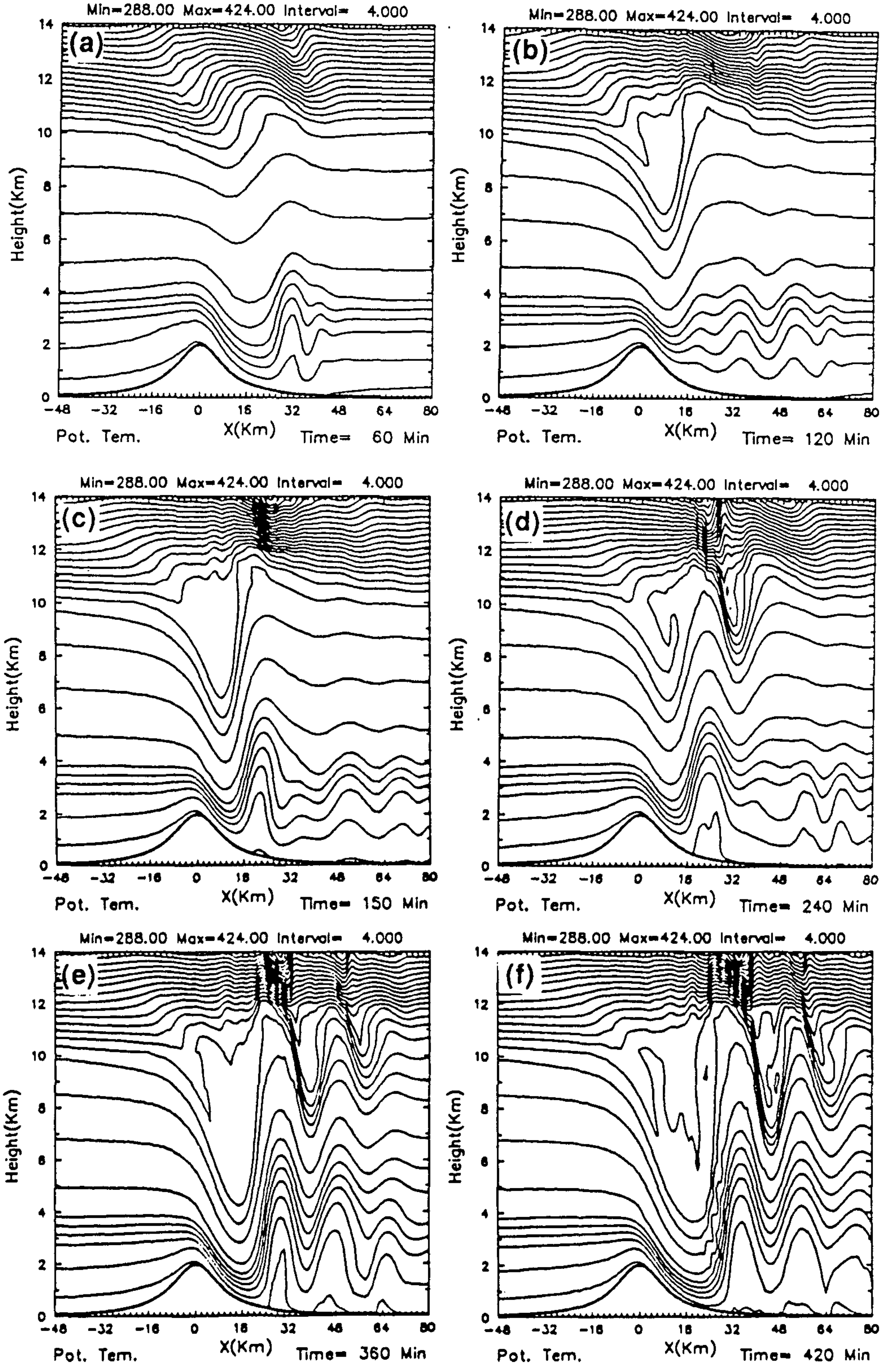

FIG. 12. The insentrope fields at various time of the model simulation of the Boulder severe windstorm.

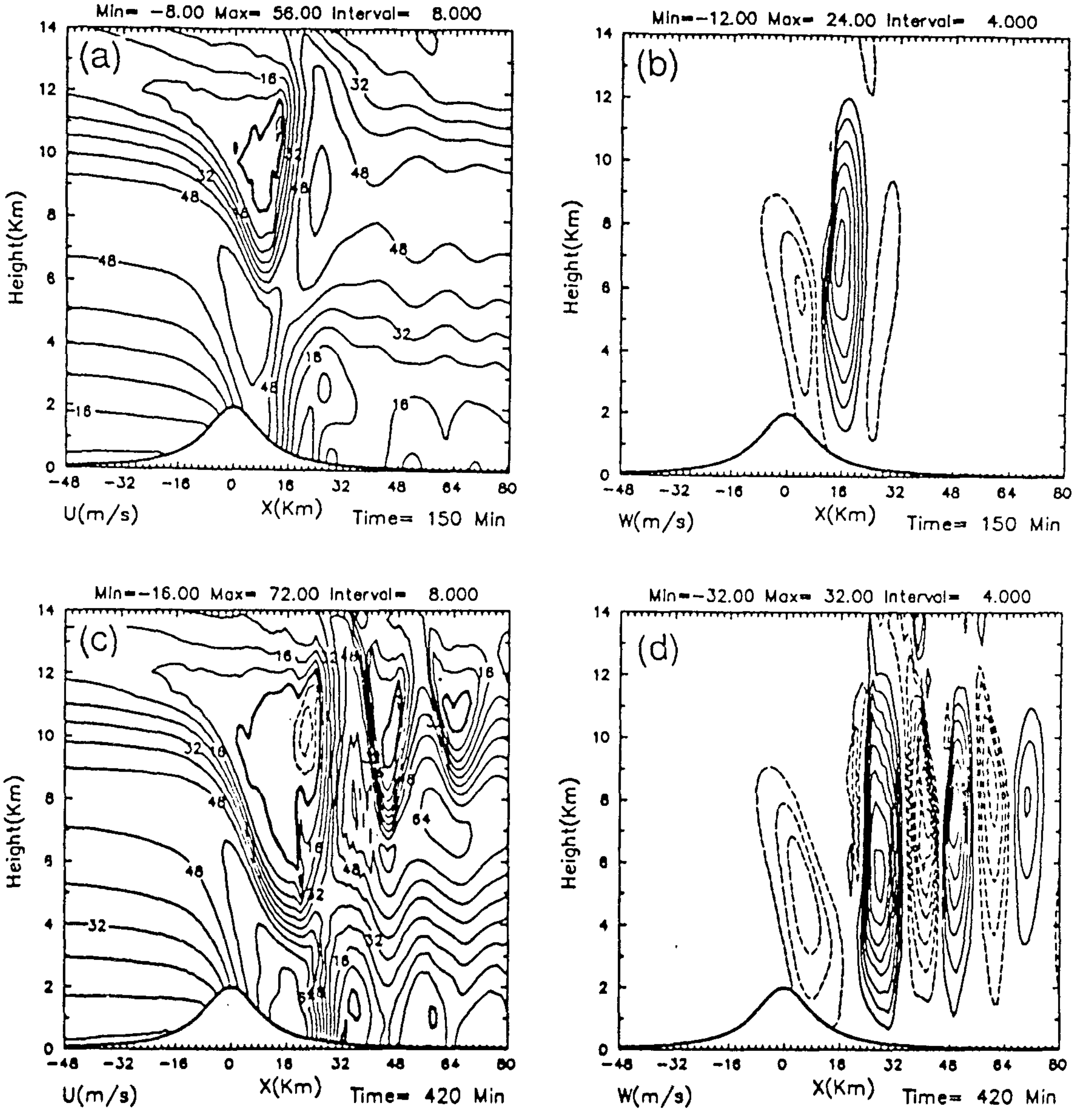

FIG. 13. The fields of horizontal velocity (left panel) and vertical velocity (right panel) from the Boulder windstorm simulation using the σ-coordinate model.

ground diffusion, but none of these was found to produce fundamental changes to the overall time evolution of the windstorm, though the timing of the development varies slightly. These results lead us to a conclusion that the development of the severe downslope wind in our model is deterministic given the upstream sounding, and the development mechanisms are well understood.

5. Conclusions

A nonhydrostatic mesoscale model is developed that makes the first practical use of the nonhydrostatic σ-coordinate equations devised by MW84. The procedure of integration is similar to that used for the anelastic terrain-following height-coordinate equations, in the sense that an elliptic equation is solved for the geopotential height. The multidimensional flux-corrected transport (FCT) scheme of Zalesak (1979) is implemented in the model to advect the potential temperature and water quantities, although its superiority over conventional schemes is not demonstrated in this paper. Here, the numerical model is verified against the linear and nonlinear analytical solutions of dry mountain waves, and an accuracy comparable to those of other established models is demonstrated. The model is also used to simulate the 11 January 1972 Boulder severe downslope wind storm and the results agree well with current understanding and recent findings on this problem. The results of model simulations also confirm the validity of the equation system as suggested by MW84, and also its potential for mesoscale modeling.

Acknowledgments. This paper is based the first author's (MX) Ph.D thesis at Reading University, which was supported by the Chinese government and the British Council under the Technical Cooperation Award. Suggestions from Drs. M. J. Miller and B. Johns on the model aspects are gratefully acknowledged. The computing facilities provided by University of London, Rutherford Appleton Laboratory, and University of Reading Computer Centers are deeply appreciated. Dr. R. Saktreger is thanked for his advice on computing systems. MX wishes to thank Dr. Z.-J. Zhang for jointly developing graphic package ZXPLOT that displays the model results in this paper. The authors also thank reviewers Drs. J. B. Klemp and J. Dudhia for their suggestions that led to a clearer interpretation of the Boulder storm simulation, and an improvement in the overall paper presentation.

APPENDIX

The Right-Hand Side of Elliptic Eq. (3.10).

$$
\begin{aligned}
p_* F_\Phi = {} & -\frac{\partial}{\partial x}(\mathrm{UFLUX} - p_* D_u) \\
& + \frac{1}{p_*}\frac{\partial p_*}{\partial x}\left(1 + \sigma\frac{\partial}{\partial \sigma}\right)(\mathrm{UFLUX} - p_* D_u) \\
& + \frac{\partial}{\partial \sigma}[S(\mathrm{WFLUX} - p_* D_w)] \\
& + \left(u + \sigma\frac{\partial u}{\partial \sigma}\right)\left(\frac{1}{p_*}\frac{\partial p_*}{\partial x} - \frac{\partial}{\partial x}\right)\frac{\partial p_*}{\partial t} \\
& - p_*\frac{\partial}{\partial \sigma}\left[gS\left(\frac{\theta'}{\theta_s} + 0.61 q_v' - q_c - q_v\right)\right] \\
& + p_t\Bigg[\left(p_*\dot{\sigma} + \sigma\frac{dp_*}{dt}\right)p^{-2} \\
& - \frac{1}{p_* p}\left(\frac{\partial p_*\dot{\sigma}}{\partial \sigma} + \sigma\frac{\partial u}{\partial \sigma}\frac{\partial p_*}{\partial x} + \frac{dp_*}{dt}\right)\Bigg]\frac{\partial p_*}{\partial t} \\
& \qquad\qquad - \frac{\partial}{\partial t}\left(\frac{\partial p_*}{\partial t} + \frac{\partial p_* u}{\partial x} + \frac{\partial p_*\dot{\sigma}}{\partial \sigma}\right).
\end{aligned}
$$

REFERENCES

Alaka, M. A., Ed., 1960: *The Airflow over Mountains.* WMO Tech. Rep. 34, 135 pp.

Anthes, R. A., and T. T. Warner, 1978: Development of hydrodynamic models suitable for air pollution and other mesometeorological studies. *Mon. Wea. Rev.,* **106,** 1045–1078.

Arakawa, A., and V. R. Lamb, 1977: Computational design of the basic dynamical processes of the UCLA general circulating model. *Methods in Computational Physics,* **17,** 174–265.

Asselin, R., 1972: Frequency filter for time integrations. *Mon. Wea. Rev.,* **100,** 487–490.

Bretherton, F. P., 1969: Momentum transport by gravity waves, *Quart. J. Roy. Meteor. Soc.,* **95,** 213–243.

Clark, T. L., 1977: A small-scale dynamical model using a terrain-following coordinate transformation. *J. Comput. Phys.,* **24,** 186–215.

Deardorff, J. W., 1971: On the magnitude of the subgrid-scale eddy coefficient. *J. Comput. Phys.,* **7,** 120–133.

Durran, D. R., 1986: Another look at the downslope windstorms. Part I: On the development of analogue to supercritical flow in an infinitely deep, continuously stratified fluid. *J. Atmos. Sci.,* **43,** 2527–2543.

——, and J. B. Klemp, 1983: A compressible model for the simulation of moist mountain waves. *Mon. Wea. Rev.,* **111,** 2341–2361.

Eliassen, A., 1949: The quasi-static equation of motion with pressure as independent variable. *Geophs. Publ.,* **17,** 1–44.

Eliassen, A. E., and E. Palm, 1960: On the transfer of energy in stationary mountain waves. *Geofys. Publ.,* **22,** 1–33.

Haltiner, G. J., and R. T. Williams, 1980: *Numerical Prediction and Dynamic Meteorology,* 2nd ed. J. Wiley and Sons, 477 pp.

Hoskins, B. J., and A. J. Simmons, 1975: A multi-layer spectral model and the semi-implicit method. *Quart. J. Roy. Meteor. Soc.,* **101,** 637–655.

Kessler, E., 1969: On the distribution and continuity of water substance in atmospheric circulation. *Meteor. Monogr.,* **32,** 84 pp.

Klemp, J. B., and D. R. Durran, 1983: An upper boundary condition permitting internal gravity wave radiation in numerical mesoscale models. *Mon. Wea. Rev.,* **111,** 430–444.

——, and D. K. Lilly, 1975: The dynamics of wave induced downslope winds. *J. Atmos. Sci.,* **32,** 320–339.

——, and ——, 1978: Numerical simulation of hydrostatic mountain waves. *J. Atmos. Sci.,* **35,** 78–107.

——, and R. B. Wilhelmson, 1978: The simulation of three-dimensional convective storm dynamics. *J. Atmos. Sci.,* **35,** 1070–1096.

——, and D. K. Lilly, 1980: Mountain waves and momentum flux. GARP. Publ. Ser., No. 23, ICSU/WMO, 116–141.

Laprise, R. J., and W. R. Peltier, 1989a: The linear stability of nonlinear mountain waves: Implications for the understanding of severe downslope windstorms. *J. Atmos. Sci.,* **46,** 545–564.

——, and ——, 1989b: The structure and energetics of transient eddies in a numerical simulation of breaking mountain waves. *J. Atmos. Sci.,* **46,** 565–585.

——, and ——, 1989c: On the structural characteristics of steady finite amplitude mountain waves over a bell-shaped topography. *J. Atmos. Sci.,* **46,** 586–595.

Lilly, D. K., 1962: On the numerical simulation of buoyant convection. *Tellus,* **14,** 148–172.

——, 1964: Numerical solution for the shape-preserving two-dimensional thermal convection element, *J. Atmos. Sci.,* **21,** 83–98.

——, 1978: A severe downslope windstorm and aircraft turbulence induced by a mountain wave. *J. Atmos. Sci.,* **35,** 59–77.

——, and E. J. Zipser, 1972: The front range windstorm of January 1972—A Meteorological narrative. *Weatherwise,* **25,** 56–63.

——, and J. B. Klemp, 1979: The effects of terrain shape on nonlinear hydrostatic mountain waves. *J. Fluid Mech.,* **95,** 241–261.

Long, R. R., 1953: Some aspects of the flow of stratified fluids: Part I: A theoretical investigation. *Tellus,* **5,** 42–58.

Miles, J. W., and H. E. Huppert, 1969: Lee waves in a stratified flow. Part IV: Perturbation approximation. *J. Fluid Mech.,* **35,** 497–525.

Miller, M. J., 1974: On the use of pressure as vertical coordinate in modelling convection. *Quart. J. Roy. Meteor. Soc.,* **100,** 155–162.

——, and R. P. Pearce, 1974: A three-dimensional primitive-equation model of cumulonimbus convection. *Quart. J. Roy. Meteor. Soc.,* **100,** 133–154.

——, and A. J. Thorpe, 1981: Radiation conditions for the lateral boundaries of limited-area numerical models. *Quart. J. Roy. Meteor. Soc.*, **107**, 615–628.

——, and A. A. White, 1984: On the nonhydrostatic equations in pressure and sigma coordinates. *Quart. J. Roy. Meteor. Soc.*, **110**, 515–533.

Moncrieff, M. W., and M. J. Miller, 1976: The dynamics and simulation of tropical cumulonimbus and squall lines. *Quart. J. Roy. Meteor. Soc.*, **102**, 373–394.

Ogura, Y., and N. A. Phillips, 1962: A scale analysis of deep and shallow convection in the atmosphere. *J. Atmos. Sci.*, **19**, 173–179.

Orlanski, I., 1976: A simple boundary condition for unbounded hyperbolic flows. *J. Comput. Phys.*, **21**, 251–269.

Peltier, W. R., and T. L. Clark, 1979: The evolution and stability of finite-amplitude mountain waves: Part II: Surface wave drag and severe downslope windstorms. *J. Atmos. Sci.*, **36**, 1498–1529.

——, and ——, 1983: Nonlinear mountain waves in two and three spatial dimensions. *Quart. J. Roy. Meteor. Soc.*, **109**, 527–548.

Phillips, N. A., 1957: A coordinate system having some special advantages for numerical forecasting. *J. Meteor.*, **14**, 184–185.

Queney, P., 1948: The problem of airflow over mountains: A summary of theoretical studies. *Bull. Amer. Meteor. Soc.*, **29**, 16–26.

Robert, A. J., 1966: The integration of a low-order spectral form of the primitive meteorological equations. *J. Meteor. Soc. Japan*, **44**, 237–245.

Scinocca, J. F., and W. R. Peltier, 1989: Pulsating downslope windstorms. *J. Atmos. Sci.*, **46**, 2885–2914.

Shuman, F. G., 1962: Numerical experiments with the primitive equations. *Proc. International Symp. on Numerical Weather Prediction*, Tokyo, Meteor. Soc. Japan, 85–107.

Smagorinsky, J., 1963: General circulation experiments with primitive equations: Part I: The basic experiment. *Mon. Wea. Rev.*, **91**, 99–165.

Smith, R. B., 1979: The influence of mountains on the atmosphere. *Adv. Geophys.*, **21**, 87–230.

——, 1985: On severe downslope winds. *J. Atmos. Sci.*, **42**, 2597–2603.

Tapp, M. C., and P. W. White, 1976: A nonhydrostatic mesoscale model. *Quart. J. Roy. Meteor. Soc.*, **102**, 277–296.

Thorpe, A. J., M. J. Miller and M. W. Moncreiff, 1982: Two-dimensional convection in non-constant shear: A model of midlatitude squall lines. *Quart. J. Roy. Meteor. Soc.*, **108**, 739–762.

Wilhelmson, R. B., and Y. Ogura, 1972: The pressure perturbation and the numerical modelling of a cloud. *J. Atmos. Sci.*, **29**, 1295–1307.

Xue, M., 1989: A nonhydrostatic numerical model in σ coordinates and simulations of mesoscale phenomena. Ph.D. thesis, University of Reading, Reading, U.K., 258 pp.

Zalesak, S. T., 1979: Fully multidimensional flux-corrected transport algorithms for fluids. *J. Comput. Phys.*, **31**, 336–362.